Bulletin of Volcanology (2024) 86:17
https://doi.org/10.1007/s00445-024-01703-1

RESEARCH ARTICLE

Three-dimensional turbulent velocity field and air entrainment of the 22 March 1944 Vesuvius eruption plume

Benjamin J. Andrews[1] · **Allie N. Coonin**[2]

Received: 4 October 2021 / Accepted: 5 January 2024 / Published online: 27 January 2024

Abstract

Turbulent air entrainment into explosive volcanic jets determines whether an eruption will produce buoyant plumes, pyroclastic density currents, or both. Most previous studies of entrainment consist of numerical models and analog laboratory experiments, with relatively few observations of natural eruptions. The existing observations of entrainment are generally time- and space-averaged measurements, which do not provide information regarding the mechanisms of entrainment. We investigate spatial and temporal variations in entrainment of the March 22 Plinian phase of the 1944 eruption of Mt. Vesuvius using a feature tracking velocimetry (FTV) algorithm applied to film collected by the U.S. Navy and digitized by the U.S. National Archives. We describe a novel technique to estimate the 3D plume morphology from normalized brightness. Projection of the 2D velocity fields from the FTV algorithm onto those 3D surfaces provides 3D velocity fields. The divergence of the velocity fields quantifies local expansion and entrainment and shows that although kilometer scale eddies are present in the plume, entrainment and expansion occur over length scales on the order of hundreds of meters. Integrating the inward directed velocities over the entraining regions quantifies local air entrainment rates. We find that entrainment of 5.4–6.1 × 10^7 m^3s^{-1} air occurs over about one-third of the observed plume margins, yielding an average entrainment velocity of ~ 2.8 ms^{-1}. Extrapolation of those rates to the entire plume indicates total entrainment of 1–3 × 10^8 m^3s^{-1}. The entrainment velocity has a magnitude ~ 6% of the magnitude of the turbulence intensity along the plume margins, indicating that the latter may approximate the centerline plume velocity and suggesting use of entrainment coefficient of 0.06 for this and similar eruptions, i.e., strong plumes with a relatively high momentum-dominated region.

Keywords Plinian eruption · Turbulence · Air entrainment · Image analysis · Plume dynamics

Introduction

Volcanic eruption columns are turbulent, multiphase, non-isothermal mixtures of gas, pyroclasts, water vapor, aerosols, and +/- ice. Whether these mixtures rise as buoyant plumes or collapse as pyroclastic density currents (PDCs) depends upon the spatial and temporal evolution of column density (e.g., Neri et al. 2003; Sparks 1986; Wilson et al. 1978). The initial mixture of gas and pyroclasts is denser than the ambient atmosphere, but is significantly hotter and erupted at high velocity. As a result, shear between the erupting jet and atmosphere results in turbulent mixing ("entrainment") of air. Incorporation, heating, and expansion of that air leads to a reduction in column density. If upward momentum of the erupting jet is exhausted before the mixture density becomes less than that of the ambient air, the column will collapse to form PDCs, whereas if the column becomes buoyant, it will form a convecting plume that rises through the atmosphere to its height of neutral buoyancy. Importantly, eruption columns can also simultaneously generate buoyant plumes and non-buoyant PDCs (e.g., Andrews et al. 2007; Andrews and Gardner 2009; Christiansen and Peterson 1981; Criswell 1987; Scott et al. 1996). Turbulent entrainment controls density evolution and thus column behavior. Improved knowledge of entrainment processes has implications for interpretation of natural volcanic eruptions as well as plume models used to forecast

Editorial responsibility: J. Dufek

✉ Benjamin J. Andrews
andrewsb@si.edu

[1] Global Volcanism Program, Smithsonian Institution National Museum of Natural History, Washington, DC, USA

[2] Department of Earth, Environmental, and Planetary Sciences, Brown University, Providence, RI 02912, USA

ash dispersal (e.g., Mastin 2007; Mastin et al. 2013; Mastin et al. 2022). Although columns are often treated as having uniform cross-sectional densities and temperatures as a function of height (e.g., Ishimine 2007; Mastin 2007; Sparks 1986; Wilson et al. 1978; Woods 1988), column properties can vary substantially at a given height because turbulence entrains and mixes air throughout the column stochastically. This is shown in experimental and numerical studies indicating substantial radial and/or azimuthal variations in column properties (Carazzo and Jellinek 2012; Esposti Ongaro and Cerminara 2016; Jessop et al. 2016; Neri et al. 2003; Neri and Dobran 1994; Suzuki et al. 2005; Suzuki and Koyaguchi 2015) and by observations of natural eruptions and their deposits showing simultaneous eruption of buoyant plumes and non-buoyant pyroclastic density currents (e.g., Andrews et al. 2007; Andrews and Gardner 2009; Christiansen and Peterson 1981; Criswell 1987; Scott et al. 1996).

Here, we describe the velocity field and entrainment for the 22 March 1944 eruption of Mt. Vesuvius, Italy. We apply a new technique to digitized film of the eruption to obtain the 3D turbulent velocity field of the plume surface. We integrate those results through space and time to obtain measurements of the bulk volumetric air entrainment rate as well as the time and length scales of local variation in entrainment.

Background

Entrainment

The mixture of particles and gas emitted at high velocity during explosive volcanic eruptions is initially denser than air, but explosive eruptions commonly generate buoyant plumes with heights exceeding 5 km above the vent (e.g., Wilson et al. 1978; Sparks 1986; Carey and Sparks 1986; Woods 1988; Mastin et al. 2009; Mastin 2014; Pouget et al. 2016; Aubry and Jellinek 2018). This is the result of the eruption columns (or portions thereof) becoming buoyant prior to reaching the top of the momentum jet, h_j. Entrainment, heating, and expansion of air can reduce column density such that all or part of the column rises buoyantly. Numerous investigations have examined air entrainment in jets and plumes (e.g., Aubry et al. 2017a; Cerminara et al. 2016; Esposti Ongaro and Cerminara 2016; Jessop and Jellinek 2014; Kaminski et al. 2005; Saffaraval et al. 2012; Suzuki et al. 2005; Suzuki and Koyaguchi 2015). It should be noted here that most of the non-volcanological literature examining entrainment by turbulent jets focuses on the behavior in the self-similar region, which is > 20–100 vent diameters downstream of the inlet (e.g., Pope 2000; Bernard and Wallace 2002); for Plinian eruptions with vent radii > 25 m (e.g. Aubry et al. 2021; Mastin and Ghiorso 2000), self-similarity may not be established until well above h_j (e.g., Carazzo et al. 2006; Saffaraval et al. 2012); thus, entrainment may be unsteady and highly variable within the region most critical for determining column buoyancy.

Although entrainment is driven by turbulent processes that fluctuate through space and time, entrainment is generally treated as a bulk property. This commonly takes the form of the entrainment velocity, U_e:

$$U_e = \frac{V_e}{A} = \alpha U \tag{1}$$

where the quotient of volumetric rate of entrainment (V_e) and plume surface area (A) is equal to the product of the radial entrainment coefficient (α) and the characteristic plume velocity (U). Experimental and numerical studies have demonstrated that α for turbulent self-similar jets and plumes in the absence of wind is predictable and ranges between ~ 0.05 and ~ 0.17, with jets having lower values of entrainment than buoyancy-driven plumes (Aubry et al. 2017a). In the presence of wind, α becomes an "effective entrainment" coefficient and can have values that are higher than the above range, although the specific value will depend on the wind speed and will vary over different sectors of the plume (Aubry et al. 2017b). Although the entrainment coefficient is often assumed to be constant, various studies have shown that it changes as the plume rises, and the bulk entrainment can be predicted based upon the Richardson number of the plume (Aubry et al. 2017a; Carazzo et al. 2008a; Carazzo and Jellinek 2012; Esposti Ongaro and Cerminara 2016; Jessop and Jellinek 2014; Kaminski et al. 2005). The relationship between plume and entrainment velocities informs our understanding of volcanic eruption dynamics. For example, top-hat plume models can predict buoyant or collapsing column behavior as functions of various eruption parameters and established entrainment coefficients (Degruyter and Bonadonna 2013; Mastin 2007; Mastin 2014; Sparks 1986; Wilson et al. 1978). But treating an inherently unsteady process with spatiotemporal variation as a bulk property masks potentially important eruption processes that can manifest as lateral or temporal variations in column density. Those mechanisms may ultimately result in partial column collapse and the simultaneous eruption of pyroclastic density currents and a buoyant plume (e.g., Andrews et al. 2007; Christiansen and Peterson 1981; Criswell 1987; Gilchrist and Jellinek 2021; Neri et al. 2003; Neri and Dobran 1994; Scott et al. 1996; Suzuki et al. 2005). Various studies have shown that crosswinds can enhance entrainment on different sectors of the plume (e.g., Aubry et al. 2017b; Bursik 2001; Mastin 2014; Muppidi and Mahesh 2008; Suzuki and Koyaguchi 2015), causing lateral variations in entrainment that must produce lateral variations in other plume parameters.

Volcanological studies have used numerical, experimental, and natural observations to examine entrainment; each of these approaches presents distinct advantages as well as limitations. As volcanic eruption plumes are very energetic, multiphase mixtures, computational studies of their turbulent dynamics require modelling at high spatiotemporal resolution, with either a large eddy simulation approach that can allow for modelling of the entire plume, or direct numerical simulation of some subregion (e.g., Cerminara et al. 2016; Esposti Ongaro and Cerminara 2016; Neri et al. 2003; Suzuki et al. 2005). Such models can describe the timescales, length scales, and magnitudes of variation in velocity, momentum, mass or density, and temperature. Numerical simulations by Benage et al. (2016) show that entrainment and expansion in PDCs occur through transient, short wavelength features. This behavior should also occur in jets and plumes as eddy motion (mixing and expansion) occurs over a range of scales.

Foundational and more recent studies rely upon experiments to provide insight into plume dynamics (e.g., Carazzo and Jellinek 2012; Chen and Rodi 1980; Hewett et al. 1971; Jessop and Jellinek 2014; Morton et al. 1956). Achieving experimental scaling applicable to volcanic eruptions is often challenging as eruption plumes have very high Reynolds numbers ($Re > 4 \times 10^7$; Burgisser et al. 2005) and comprise turbulent suspensions of hot particles in air; laboratory constraints typically limit Re to $<< 10^5$, with many experiments conducted in aqueous apparatus (e.g., Aubry et al. 2017a; Aubry et al. 2017b; Carazzo et al. 2014; Carazzo and Jellinek 2012; Jessop et al. 2016; Veitch and Woods 2000), although a more limited number of investigations have used particle laden experiments with air as the ambient fluid (e.g., Benage et al. 2019; Saffaraval et al. 2012). At the grossest scale, these experiments have demonstrated different regimes of activity from weak to strong plumes (e.g., Aubry et al. 2017b), and collapsing, partially collapsed, or buoyant columns (e.g., Carazzo and Jellinek 2012; Gilchrist and Jellinek 2021). Experiments have described the entrainment coefficient (e.g., Jessop and Jellinek 2014; Morton et al. 1956), effects of overpressure on that coefficient (Saffaraval et al. 2012), and the potential for crosswinds to enhance entrainment (Devenish et al. 2010; Degruyter and Bonadonna 2013; Carazzo et al. 2014; Aubry et al. 2017b). Other studies have explored particle sedimentation from different portions of the plume, reentrainment of these particles back into the column (Carazzo and Jellinek 2012; Veitch and Woods 2000), and vent geometry (Jessop et al. 2016).

Natural eruptions pose physical hazards that limit safe observation, and large eruptions do not often occur with sufficient lead times to allow for systematic filming and instrumental observations of eruption columns. Acknowledging those limitations, various studies have used photographic or motion picture observations of plumes to describe eruption behavior and entrainment (e.g., Andrews and Gardner 2009; Sparks and Wilson 1982; Woods and Kienle 1994). As an example, Sparks and Wilson (1982) used observations of the 1979 Soufriere St. Vincent eruption to describe rise speeds, acceleration, and spreading angle of the plumes, which can describe an average entrainment coefficient. Further, only the exteriors of real eruption columns can generally be observed. Sparks and Wilson (1982) used the rise speed of the plume front to estimate the interior velocity structure following the scaling relationships of Turner (1962). Andrews and Gardner (2009) used the turbulent velocity field of the 18 May 1980 Mount St. Helens plume to infer the interior plume structure and lateral variations in entrainment and mixing; they did not, however, measure entrainment. More recently, Aubry and Jellinek (2018) have estimated entrainment values by tuning entrainment parameters of numerical models to observations of natural eruption rate, plume height, and atmospheric conditions, and Bombrun et al. (2018) have used thermal camera observations of natural eruption plumes to estimate entrainment. To date, no estimates of entrainment in natural eruption columns have been made using turbulent 3D geometries.

March 1944 eruption of Vesuvius

Mt. Vesuvius has 26 confirmed eruptive intervals between 1631 and 1944, with VEI5 and VEI4 eruptions in 1631 and 1874, respectively (GVP 2013). The most recent interval of eruption began on 5 July 1913 and ended on 7 April 1944. Vesuvius has not since erupted.

Cole and Scarpatti (2010) use the contemporary descriptions of the eruption made by Giuseppe Imbo and more recent field data to develop a detailed reconstruction of the explosive activity that occurred between 18 March and 4 April 1944. Following Imbo, they divide the eruption into four phases. Phase 1 began when lava effusion destroyed and rebuilt a small cone within the summit crater several times before ultimately filling the crater and sending lava flows to the N and SSE. Phase 2 initiated at 1715 (local time) on 21 March with the eruption of lava fountains to heights of ~ 1 km. Eight successive lava fountains erupted over the next ~ 19 h, with the final one finishing before 1240 on 22 March. Phase 3 of the eruption began shortly after 1200 on 22 March with eruption of an ash column. Explosive activity continued until ~ 1755, when it paused for ~3 h before resuming ash eruption from two vents at 2100 and then continuing until ~ 1400 on 23 March. Phase 4 of the eruption was characterized by discontinuous eruption of an ash column; the intensity of the eruption waned during this phase and became more intermittent. Imbo's historical records report that the paroxysmal activity ended on 31 March. Pyroclastic density currents were generated at various times during Phases 3 and 4, with some reaching more than 2 km from the vent.

This study focuses on Phase 3 of the eruption. During this phase, Cole and Scarpatti (2010) report that aviators at the nearby Capodichino airport estimated a column height exceeding 5000 m above sea level during the afternoon of 22 March. Using the method of Carey and Sparks (1986), they report an umbrella cloud height > 10 km above sea level based upon their own clast isopleth maps, and they estimate a crosswind speed of ~ 20–50 m/s acting to disperse the eruption plume at altitude. In contrast, Cubellis et al. (2016) assess column height using ash dispersal maps and measured crosswind speeds of 2–18 m/s to inform a numerical model of plume rise and ash dispersal. Cubellis et al. report that ashfall < 100 km from Vesuvius is best explained by a ~ 5-km column but more distal deposits require an 8–10-km tall eruption column. They suggest that bimodality may reflect a rapid increase in the height of the eruption column during Phase 3. The discrepancy between the contemporary estimates of column height made by aviators (with experience estimating altitude) and those made using clast dispersal illustrates the uncertainties that often exist in values for even more easily attainable plume parameters like column height.

Methods

Film for this study was obtained from the United States National Archives. The 35-mm, 24 frame per second film was collected by the U.S. Department of the Navy in 1944, and then transferred to the Archives. The film was digitized at the highest resolution possible in 2017, resulting in 10-bit grayscale 3112 × 4096 pixel images in .DPX format. We processed those images using MATLAB to

1) identify separate sequences within the film
2) remove or compensate for camera movement
3) estimate the three-dimensional surface structure of the plumes
4) quantify the two-dimensional velocity field
5) determine the 3D velocity and entrainment fields of the plume surface
6) quantify turbulent time and length scales
7) determine the image scaling

The following subsections present these methods in a cursory manner, Supplement 1 presents them in detail.

Identification of image sequences

As the film comprises a series of sequences collected from different vantage points, we identified contiguous clips to facilitate image processing and analysis. Once each sequence was identified, we then focused our analyses on two of the longest-duration clips capturing the entire eruption plume. These two clips, Clips 57 and 58, have durations of 13.6 and 41.45 s, respectively. Based upon the orientation of the sunlight in the two clips, they were collected at approximately 1500 (local time) on 23 March 1944.

Image registration

Camera motion is apparent in most clips (Supplement 2). To stabilize images, we selected 10 stationary features in the first image of each sequence that would be visible in all images within a clip. The images were then zero-padded on all sides with 200 pixels. We then used a 2D cross correlation script operating on a 101 × 101 pixel domain to register those features in subsequent images.

Scaling of images

We determine image scaling as a function of film size (35 mm), assumed lens focal length, identification of geographic features in the foreground, and measurement of the distance between those features and the vent. The film was most likely collected using an Eyemo camera with a 35-mm lens. We estimate an approximate vent width of ~ 605 m, in good agreement with the modern ~ 610 m size; this results in a scaling of 3.2 m/pixel at the plume position. Based upon focal length calculations and identification of features in the somma wall, Clips 57 and 58 were collected from ~ 13.1 km WNW of the Vesuvius vent at or near the 1944 Capodichino airport (site of the modern Aeroporto Internazionale di Napoli); the camera was oriented towards the volcano with a bearing of ~ 121°. We note that whereas assuming a 25- or 50-mm lens changes the scaling of vent width to 647 or 573 m, respectively, (both of which are within ~ 6% agreement with modern measurements of the rim), changing to longer focal lengths results in vent sizes that are > 10% too small. Further, focal lengths of 75- or 152-mm suggest camera positions ~ 25 or ~ 50 km from Vesuvius, both of which are unlikely. Scaling values are presented in Table 1.

Table 1 Surface reconstruction and feature-tracking velocimetry parameters. Sun angle and camera azimuth is given with in degrees from north and above the horizon (sun only). FTV parameters are reported in pixels for the smaller window size, R, and grid spacing used to assess small turbulent structures as well as the larger sizes used for examining bulk behavior. The durations of Clips 57 and 58 are 327 and 996 frames, respectively (equivalent at 24 frames per second to ~ 13.6 and ~ 41.5 s)

Sun angle (Az./Elev.)	Camera azimuth	FTV Turb (R/Grid)	FTV large (R/Grid)	Scale (m/pix)
249°/24°	121°	25/6	181/45	3.2

3D plume surface morphology

The 3D surface morphology of the plume is estimated using a novel technique that assumes the grayscale brightness of the plume is a function of the orientation of the plume surface to the incident light; portions of the plume normal to the incident sunlight are white, whereas those oriented away from the sun are dark. The method is conceptually similar to the gradient method for surface reconstruction described by Harker and O'Leary (2013), but as the plume geometry is more poorly defined *a priori* than the industrial surfaces examined by those authors, we require a different approach. Our technique assumes that the plume has a uniform color and is Lambertian (i.e., brightness is not dependent on viewing angle, but only on the angle between the surface and incident light). Required inputs are the camera orientation and sun orientation; we estimate the former through comparison of the images with topographic maps and the latter through the NOAA Solar Position Calculator using inputs of 1500 local time and 22 March 1944. This time is estimated from inspection of the relative angle between the camera view and lighting, and consideration of eruption chronology (Cole and Scarpatti 2010); the angles of the sun and camera are reported in Table 1. Together those angles define the unit vector of the incident sunlight with respect to the imaging plane. The program then assumes an initial surface Z normal to the camera viewing angle and calculates the normal vectors to that surface at all positions; the dot product of those vectors and the incident light is the calculated image brightness at each point within the pixel grid. The program uses the difference between this calculated image and the original image to change the positions of surface Z with respect to the camera: regions that are too bright are moved away from the camera and those not bright enough are moved towards the camera (thereby increasing or decreasing, respectively, the angle between the incident light and the surface). That process is repeated for each frame starting with a surface $Z = 0$. We evaluated the precision of this technique by applying it to a sphere of known radius (Fig. 1); we find that the method is accurate to within < 5% of the actual radius and ~10° of the surface angle, provided the angle between the incident light and surface normal is < 45°; about 70% of the imaged plume surface meets the <45° condition, but we note that we only observe one side of the plume. Supplement 1 contains additional detail of surface geometry calculations and shows examples of final surfaces.

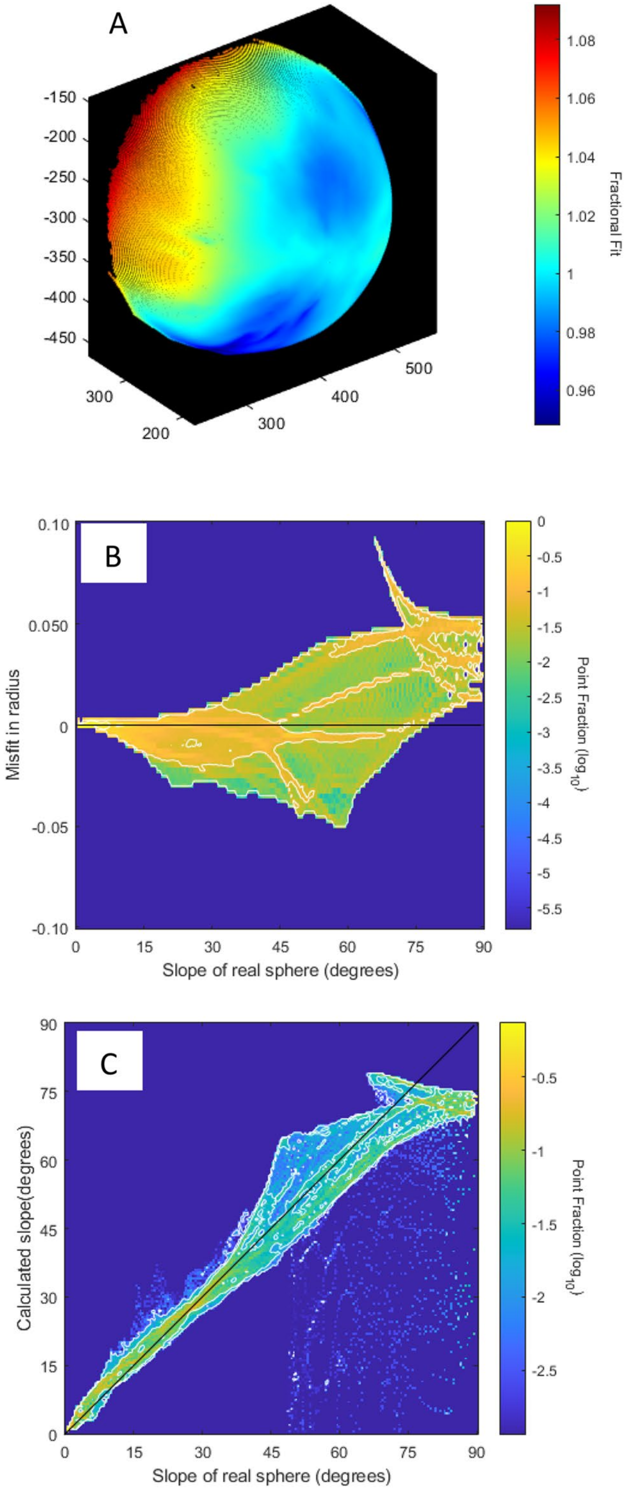

Fig. 1 **A** Surface reconstruction of sphere. Colors indicate the ratio of the reconstructed radius to the actual radius ("misfit"). Pixel scaling indicated as *x*-, *y*-, and *z*-axes. **B** Radial misfit as a function of sphere surface slope with respect to the viewing angle. **C** Calculated versus actual slope of the sphere

2D feature-tracking-velocimetry

We obtain 2D velocity fields of the plumes using a feature-tracking-velocimetry (FTV) program written for Matlab (Andrews 2014; Andrews 2019). Briefly, we used window sizes of 25 and 181 pixels for studying turbulent and bulk behaviors, respectively; those window sizes were chosen by calculating velocity fields for window sizes ranging from 11 to 251 pixels for nine positions (one grid point and eight nearest-neighbors) for the entire time series, and then determining the smallest window size at which anomalously large vectors are no longer present, and a larger size at which low-frequency variations in velocity first appear. Velocity fields are calculated for each pair of frames. The resulting velocities were filtered using a nearest neighbor scheme, and any velocities > 210 m/s were discarded; this threshold corresponds to motion exceeds 3 pixels per frame, and inspection of the film sequences shows that any detected motion exceeding that threshold is not real. The program is described in more detail in Supplement 1. All parameters used in the FTV analyses are reported in Table 1.

3D velocity and entrainment fields

The 3D velocity field is determined by projecting the 2D velocity field onto the 3D surface morphology. Specifically, the gradient of the surface, ∇Z, is evaluated at each point for which a velocity exists. The magnitude of the component of velocity parallel to the camera view (w) is given as

$$w = [u, v] \bullet \nabla Z \tag{2}$$

Uncertainty in w scales with uncertainty in the slope of the calculated surface Z.

The divergence of the 2D velocity field indicates regions of expansion (positive divergence) or entrainment (negative divergence). The integral of the velocity component perpendicular to the surface over each entraining region provides the volumetric entrainment rate into the plume for that region. The sum of those fluxes is the entrainment rate for the entire plume, and the ratio of that rate to the plume surface area is the average entrainment velocity. An approximation of the local entrainment rates can be made by integrating the 2D divergence over each entraining region.

Turbulent timescales and length scales

We examined the turbulent integral timescales and length scales of the plume through standard autocorrelation techniques to describe the largest turbulent structures (e.g., Pope 2000; Bernard and Wallace 2002; Andrews et al. 2011; Andrews and Manga 2012; Andrews 2014), which have length scales on the order of 1000 m. Importantly, even in analyzing the longest contiguous clip (41.45 s duration) the timescales calculated routinely vary as a function of the duration over which they are calculated, indicating that the integral turbulent timescales of the plume margins have durations > 20 s. That is, large turbulent structures can persist for 20 s or longer.

Turbulent length scales were calculated by conducting autocorrelation analysis of approximately vertical profiles from the vent to the top of the plume. The profiles of velocity or surface geometry were detrended to remove linear shifts as a function of height. Length scales were then determined as both integrals of the autocorrelation and as the distance to zero correlation (Andrews et al. 2011).

Results

Plume descriptions and surface morphologies

The two clips analyzed in this study show the plume in its entirety (Clips 57 and 58). Figure 2 shows representative frames from each clip, and the registered films are presented in Supplemental Material 2. Clips 57 and 58 show unobstructed views of the northwest side of the rising eruption column. The plume rises to a maximum height ~ 7000 ± 250 m above the vent (about 8000 m above sea level), and the downwind ash plume seems to spread at 5000–6000 m above the vent (although this latter estimate is highly uncertain, as the plume spreads away from the camera and is mostly

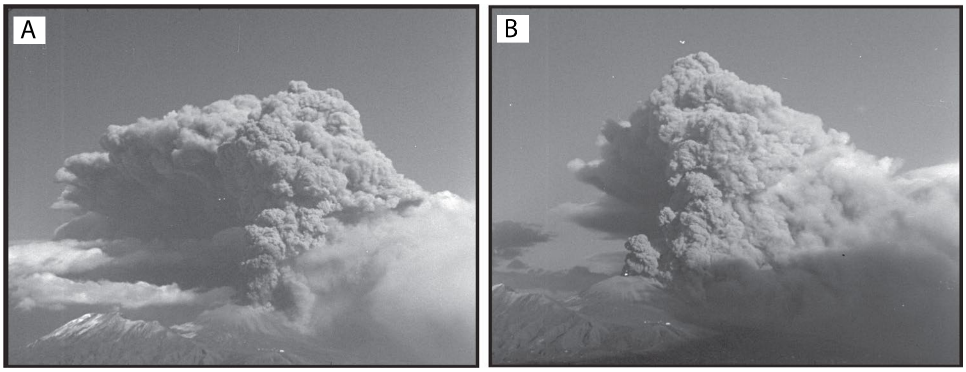

Fig. 2 Representative images of 22 March 1944 Vesuvius eruption from **A** Clip 57 and **B** Clip 58

obscured). These estimates are closer to those of Cubellis et al. (2016) than those of Cole and Scarpati (2010). The largest turbulent structures on the plume surface have length scales exceeding 500 m; these features contain a cascade of smaller scale eddies. Clip 58 captures a small PDC traveling down the south flank, and a diffuse plume rising from the same region in Clip 57 likely indicates a previous PDC. Clip 58 also shows the rise of a new, small plume from the vent; over the > 40 s clip, this new plume rises ~ 2000 m above the vent.

Figure 3 shows representative 3D plume surface reconstructions from Clip 57. Reconstructions of both clips are presented in Supplemental Material 3. Both plumes expand ~ 1000 m toward the camera as they rise from the vent to their neutral buoyancy heights at 5000–6000 m above the vent; this expansion represents a plume opening angle of ~ 10° towards the camera (in the upwind direction).

Profiles from the vent to the top of the plume surface show large-scale relief occurring at two dominant length scales (Fig. 3 and Supplement 4). In both clips, there is a noticeable shift in the plume surface away from the camera about 2000–3000 m above the vent. This shift may indicate the superposition of a subsequent plume in front of an earlier plume or one generated by pyroclastic density currents erupted down the SE flanks (away from the camera). Clip 58 supports this explanation as a vent-sourced plume rises in the foreground. Eddies on the surface of the plume have relief on the order of ~ 100 m and length scales of 400–600 m. Most of the eddies present on the plume surface do not rise rapidly, but instead remain at relatively constant vertical position with “topographic” expressions that emerge from and then recede back into the plume surface.

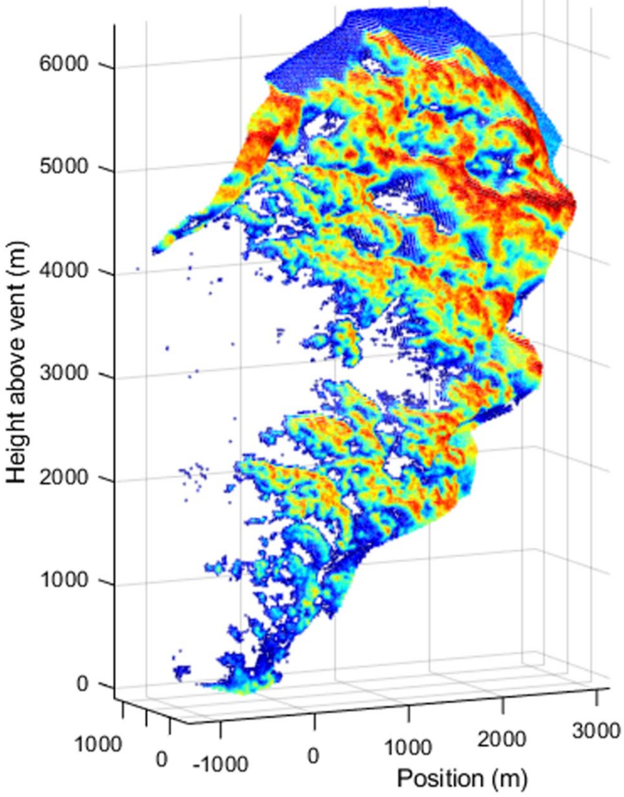

Fig. 3 Representative surface reconstruction from Clip 57 (frame 25). The surface color is set by the original image grayscale values

Turbulent velocity fields and plume rise speed

Figure 4 shows representative velocity fields from both clips. Turbulent structures occur in the velocity fields at a range of timescales and length scales, from high frequency or short wavelength features that vary over only a few frames or 10 s of pixels, to kilometer-scale features that persist for 15 s or longer.

Velocity fields calculated using the large subregions (181 pixel square) track large scale motions of the plume surface. The time-averaged vertical component of velocity is between − 5 and 5 m/s for most heights in both clips (Fig. 5). The time-averaged velocity magnitudes are much greater that the vertical components of velocity, with values of ~ 50 m/s (Fig. 5). Manual tracking of the fronts of individual rising eddies, however, shows speeds of ~ 10 m/s for eddies rising in the main portion of the plume, and up to 50 m/s for the plume in the Clip 58 foreground. Together, these observations indicate that most of the large eddies visible on the plume surface are relatively stationary, but have high rotational velocities. The faster rise speeds measured for some eddies likely coincide with rise of a new plume or turbulent structures moving from the column interior to exterior; this will be discussed in greater detail in “Plume structure and entrainment coefficient.” Note that surface velocity fields described here do not perfectly reflect the interior velocity structure of the jet; as a result, the region near the vent shows a low vertical surface velocity whereas the interior jet velocity is likely many 10s of m/s.

Figure 6 shows profiles of turbulence intensity, U’, through the plumes in Clip 57 and 58 as calculated using the small subregion (25 pixel square). The turbulent velocity U any point can be described as

$$U = \overline{U} + U' \tag{3}$$

where $\overline{U}$ is the time averaged component of velocity and U’ is the fluctuating component of velocity or turbulence intensity. In both clips, U’ is ~ 50 m/s, with a 1-σ range between 35 and 70 m/s. There does not appear to be any systematic variation in U’ with height; Clip 58 shows a slight increase in the mean with height, but the 1-σ bounds are relatively stable over the observed plume.

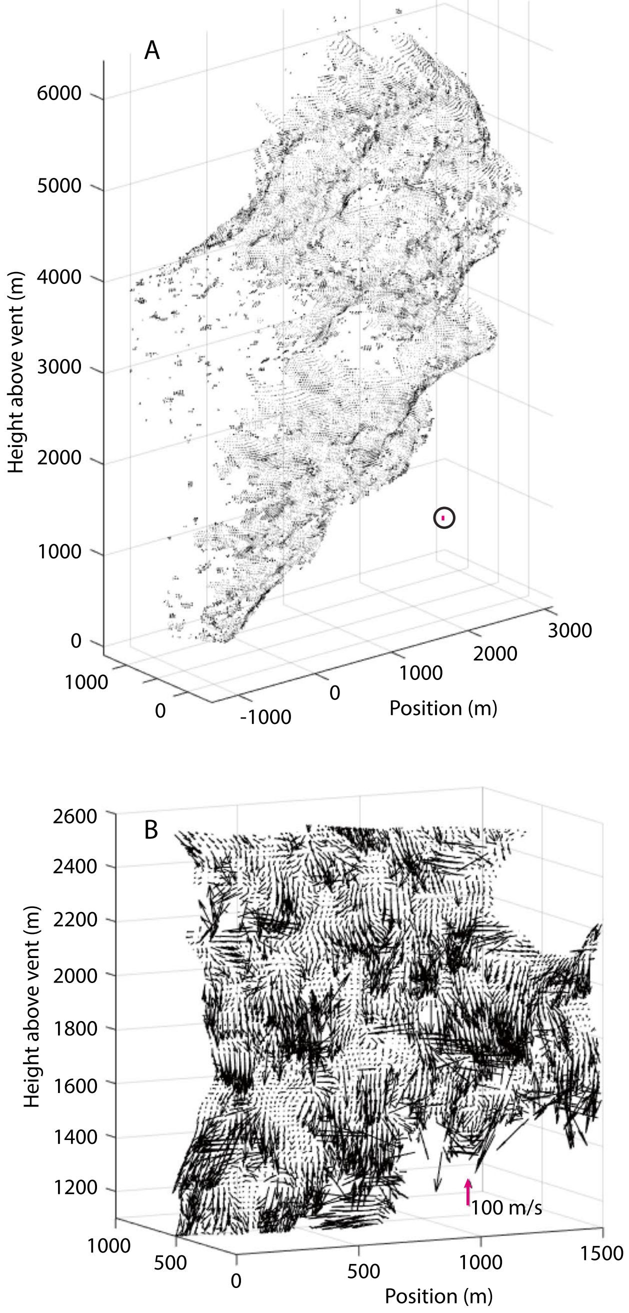

Fig. 4 **A** 3D velocity field of Clip 57 (frame 25). Small vector at position [2000, 0, 1000] indicates 100 m/s. **B** Close up view of portion panel **A** illustrating turbulent velocity field. Note vertical vector indicating 100 m/s scale

Turbulent length scales and timescales

The streamwise turbulent integral and zero-correlation length scales of the plumes are approximately 200–400 and 450–650 m, respectively, in both Clips 57 and 58. These length scales are comparable to the length scales of surface roughness in the reconstructions and profiles shown in Fig. 3.

As noted in “Turbulent timescales and length scales,” the integral timescales of the plumes are longer than 20 s and therefore the durations of the clips are too short to determine the timescales through autocorrelation calculations. These timescales can, however, be estimated from the ratio of length scale and characteristic velocity. That velocity is usually considered to be the centerline velocity of the eruption column, but as that velocity cannot be observed, we use the time-averaged velocity magnitudes as a proxy for the characteristic velocity. Turbulence on the column margins is the result of shear between the column interior and the atmosphere, and the magnitude of velocity on the plume margins should not exceed the interior velocity. We are thus confident that the marginal velocities are approximately representative of the characteristic velocity, although they may be an underestimate. The mean velocity magnitudes (~ 50 m/s) result in integral timescales on the order of approximately 4–15 s. These timescales indicate the characteristic overturn time for the largest eddies on the plume margins.

Entrainment fields, rates, and velocities

Entrainment varies substantially through space and time. Entraining features generally have wavelengths < 100 m (Fig. 7) and occur on the plume surface with no recognizable pattern. These features do not usually persist for more than a few frames (<< 1 s).

Volumetric entrainment rates and velocities are shown in Fig. 8 and time series animations of those plots are presented in Supplement 5. Clips 57 and 58 show substantial variation in entrainment rate through time and space, with the volume entrained per m of plume height ranging locally from ~ 0 to > 10^5 m^3/s in Clips 57 and 58 (Fig. 8A, E). The time averages of entrainment with height for both Clips 57 and 58 show a general increase from ~0 just above the vent to a maximum of ~ 5×10^4 m^3/s at a height of ~ 5000 m; entrainment returns to ~ 0 by 6500-m height. The increase with height is expected, as the plume surface area increases with height. The low value of entrainment near the vent is likely the result of uncertainties in our calculation of entrainment from the velocity field, challenges with shadows and potentially non-uniform eruption column color nearer the vent, and the small size of the vent region compared to the rest of the column; disambiguating those contributions is not possible with this dataset. The total time averaged entrainment measured in Clip 57 is ~ 5.4×10^7 m^3/s and in Clip 58 is ~ 6.1×10^7 m^3/s. The fraction of the plume surface area entraining ranges from < 0.1 to ~ 0.7 in both Clips 57 and 58 (Fig. 8C, G), but the time average and 1-σ bounds show entraining fractions of 0.15–0.5 (Clip

Fig. 5 **A** Average vertical velocity for Clip 57 as calculated using the large FTV window size is typically < 5 m/s. **B** Average velocity magnitude, in contrast, is an order of magnitude greater. Note that the high velocity magnitudes between 2500 and 3500 are an artifact of a lower plume in the superpositioned in front of the higher plume in the background

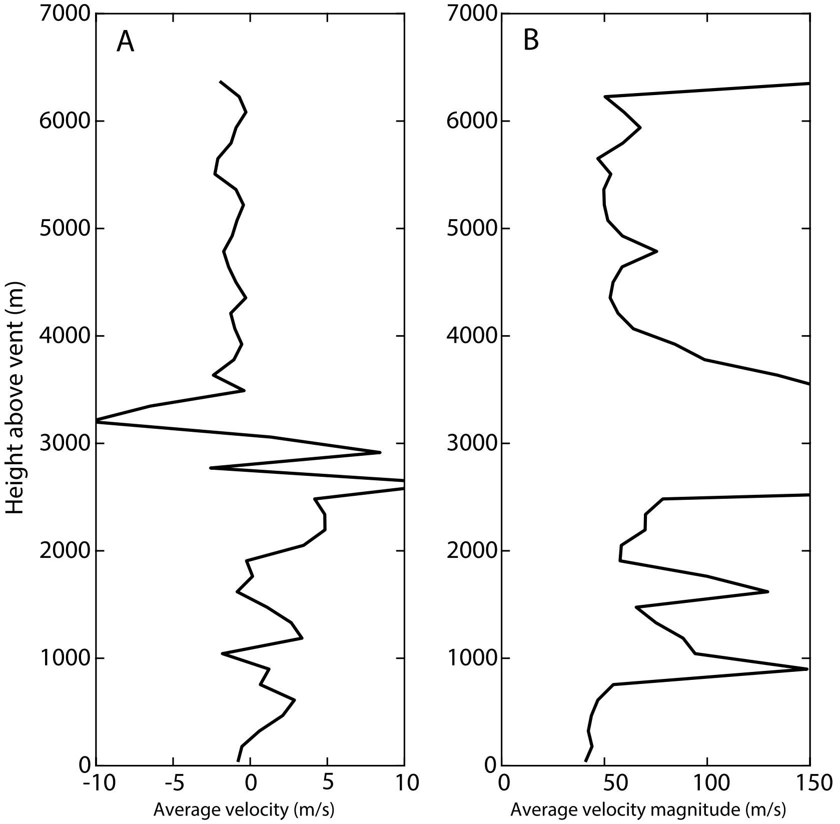

Fig. 6 Turbulence intensity as a function of height for **A** Clip 57 and **B** Clip 58. Grayscale indicates the frequency of a particular intensity at a given height. Bold line indicates the average intensity and thin lines show ±1 standard deviation

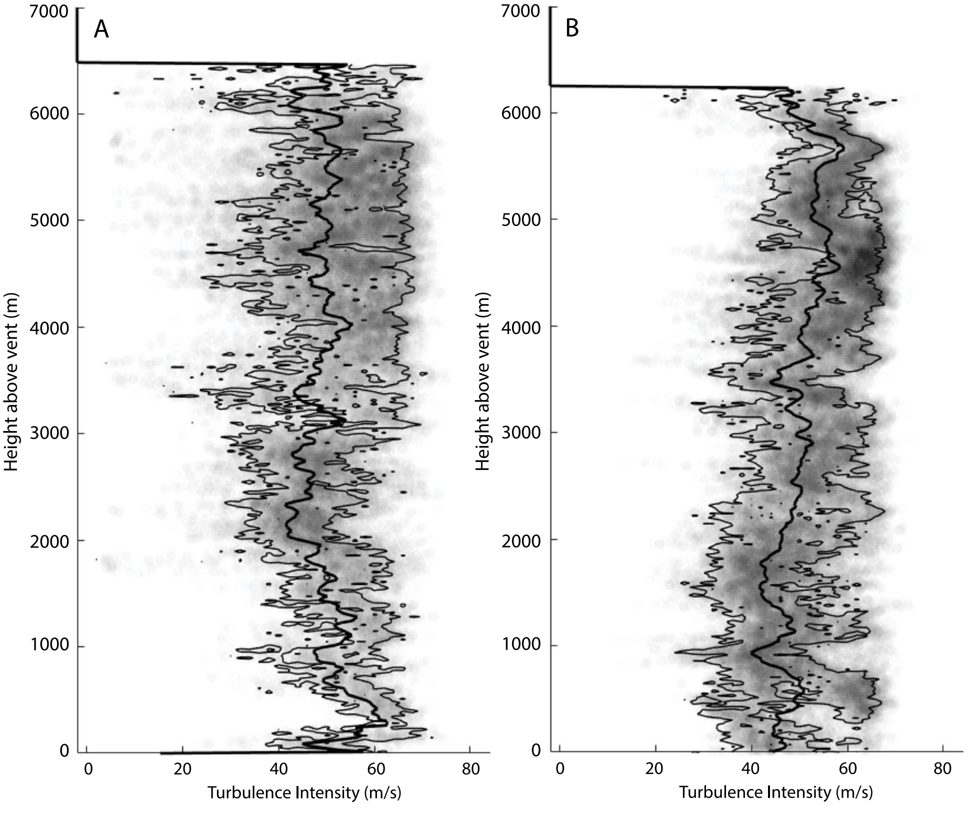

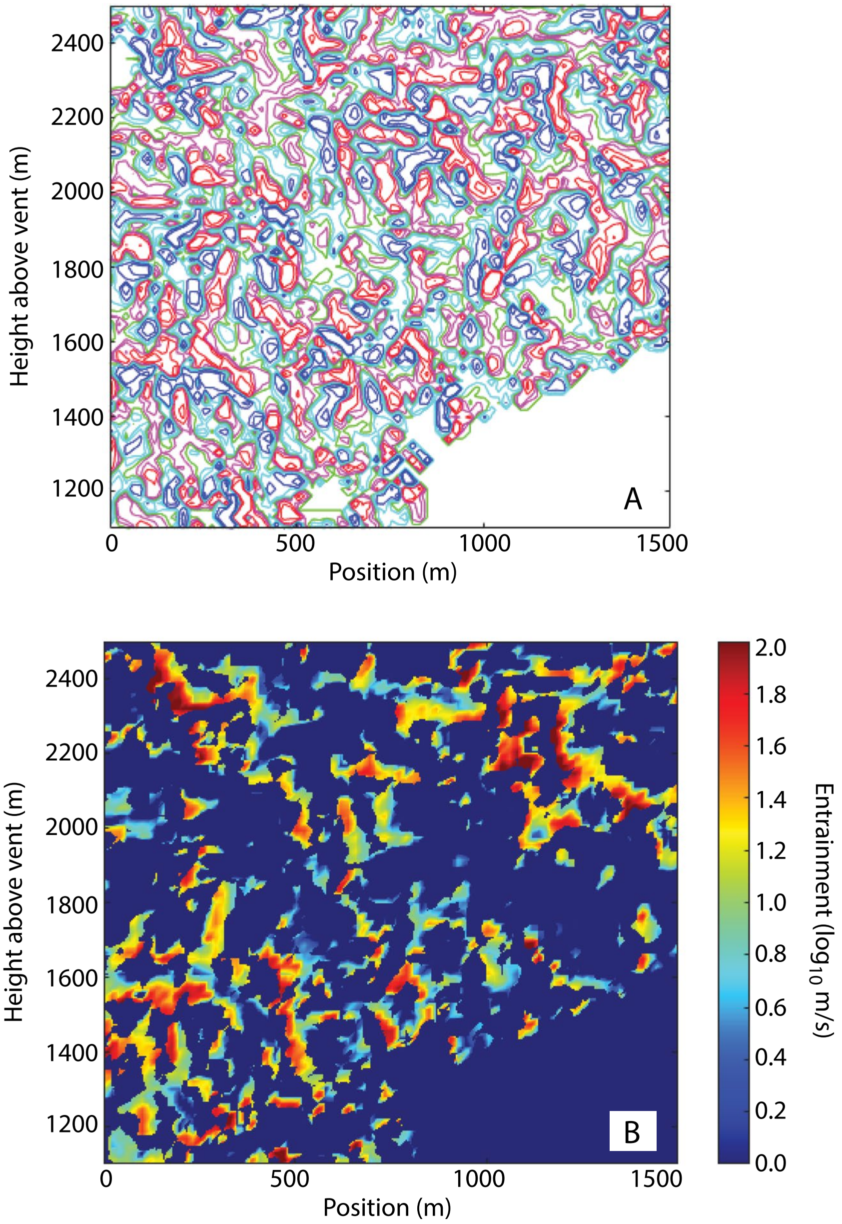

Fig. 7 **A** Divergence of 2D velocity field for Clip 57 (frame 25) for the same region shown in Fig. 4B. Red regions are entraining and blue regions are expanding. **B** Entrainment for the region shown in panel **A**

57) and 0.15-0.4 (Clip 58) over most of the plume, with full-plume averages of 0.32 for both clips. Measurements of entrainment calculated from only the divergence of the 2D velocity fields show similar patterns, but are approximately half the magnitude in both clips; a slightly higher fraction of the plume appears to be entraining in the 2D measurements (0.37 for both Clip 57 and 58).

Dividing the entrainment at each height by the unit width of the region of interest at that height (i.e., a 1500-m wide portion of the plume 1 m tall) provides the entrainment velocity as a function of height (Fig. 8B, F). Entrainment velocity ranges from ~ 0 to > 10 m/s in Clip 57, but time averaging those profiles shows a relatively constant value of ~ 2.9 m/s until a height of > 5500 m above the vent. Clip 58 shows a very similar pattern, with local variation in entrainment velocity from 0 to 10 m/s, but a near constant time-averaged value of 2.8 m/s. Calculating the average entrainment velocity U_e through time and space as the quotient of the average entrainment volume flux and plume surface area yields values of U_e of 2.9+/−0.7 and 2.8+/−0.7 m/s for Clips 57 and 58, respectively. The 2D measurements of entrainment velocity are approximately half the magnitude of the 3D measurements (1.4 and 1.3 m/s for Clips 57 and 58, respectively).

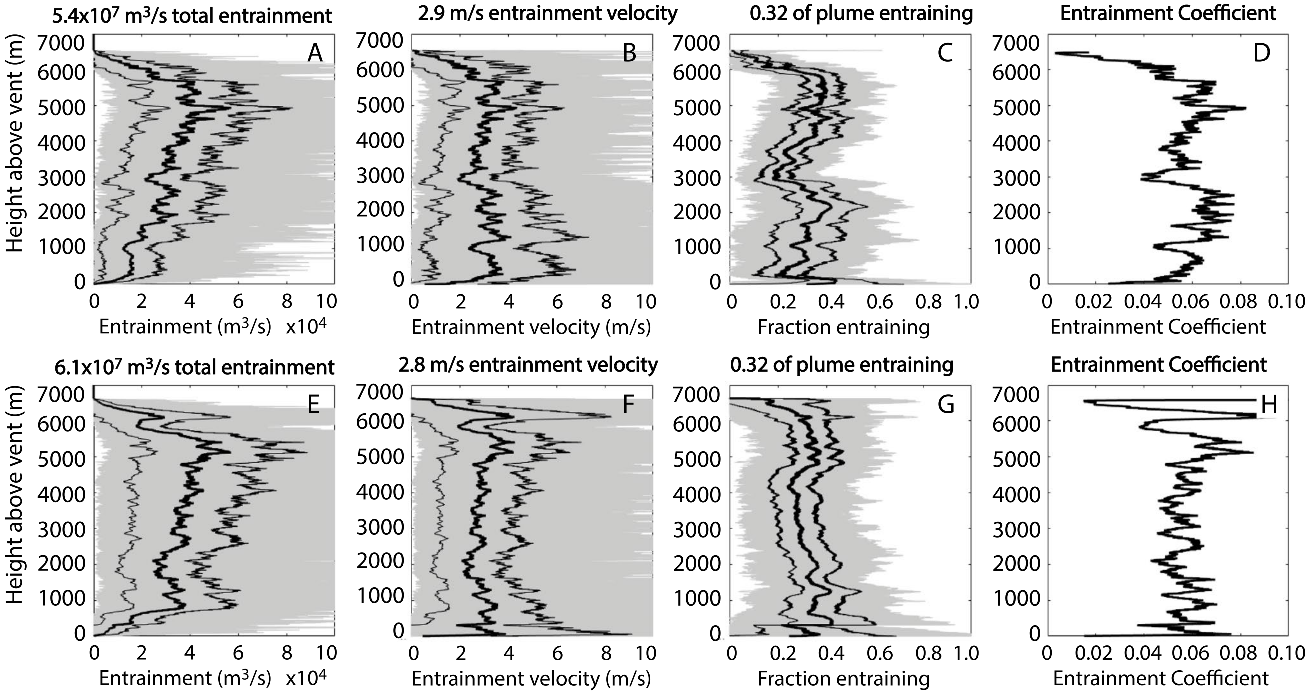

Fig. 8 **A** Entrainment into Clip 57 as a function of height. **B** Entrainment velocity for Clip 57. **C** Entraining fraction of imaged Clip 57 plume surface. **D** Entrainment coefficient ($\alpha = U_e/U'$) for Clip 57. **E** Entrainment into Clip 58. **F** Entrainment velocity for Clip 58. **G** Entraining fraction of imaged Clip 58 plume surface. **H** Entrainment coefficient ($\alpha = U_e/U'$) for Clip 58. In all panels, the gray body is the stack of individual frames, the bold black line is the time average, and the thin black lines show ± 1 σ bounds. Animated versions of panels **A**, **B**, **D**, and **E** are presented in Supplement 5

Discussion

Bulk entrainment volume flux

The bulk entrainment rates for Clips 57 and 58 range from ~ 4×10^7 to ~ 9×10^7 m^3/s, with time-averaged values of ~ 5.4×10^7 and ~ 6.1×10^7 m^3/s, respectively. Those values only measure entrainment through the ~ 90° sector of plume oriented toward the camera. Assuming that all sides of the plume entrain equally, then the total entrainment is four times the measured values, or ~ 2.2 to ~ 2.4×10^8 m^3/s; this, of course, assumes a radially symmetrical plume. But we know that the plume was not perfectly symmetrical, as winds blowing subparallel to the camera orientation dispersed the plume downwind and away from the camera. Depending on the strength of the wind relative to the plume rise speed, a crosswind can enhance entrainment on some portions of a plume, particularly on the downwind side (Aubry et al. 2017a; Muppidi and Mahesh 2008). Although we do not know the wind profile, lower or higher bounds may be estimated by incorporating the effects of wind on entrainment (Aubry et al. 2017a; Carazzo et al. 2014; Degruyter and Bonadonna 2013; Devenish et al. 2010; Suzuki and Koyaguchi 2015). Cole and Scarpatti (2010) estimate a wind speed of 20–50 m/s based upon tephra dispersal, whereas Cubellis et al. (2016) estimate a wind speed of 2–18 m/s. The uncertainties resulting from wind and the observational geometry suggest a range in total entrainment of ~ 1.5–3.5×10^8 m^3/s.

Plume structure and entrainment coefficient

Spatiotemporal variations in entrainment (e.g., Figs. 7 and 8) reflect the length scales, timescales, and intensities of turbulent eddies within the plume. Because the largest eddies advect mass from the plume center to its margins and back again, these are the structures that produce variation in density, and ultimately influence which portions of a plume may collapse. Although large turbulent structures efficiently transfer momentum from the interior to the margins and return entrained air to the interior most effectively (e.g., Pope 2000; Bernard and Wallace 2002), the entrainment field does not resolve large-scale structures but rather displays entrainment and expansion over very short length scales and timescales (Fig. 7). This high-frequency variation is not surprising, as the largest turbulent structures comprise a cascade of ever smaller features, and those smaller eddies accomplish the entrainment. The largest eddies do not manifest coherent or easily recognizable velocity fields on the plume surface, but the turbulent intensities measured on the surface may be a proxy for the centerline velocity of the plume interior.

The eddies visible in the video footage do not generally rise along the column margins, but instead turnover and re-enter the plume at relatively constant height. The rise of a plume head (as seen in Clip 58) is different than motion along the margins of the plume. Similar observations of quasi-steady eddies on the plume margins were made by Sparks and Wilson (1982) and is supported by recent jet experiments (Benage et al. 2019) where eddies rotate on the plume margins but have effectively zero rise velocity.

Entrainment velocity is assumed to be proportional to the characteristic plume (or jet) center-line velocity (Eq. 2). In plume models, this relationship can be exploited to calculate the time-averaged rate at which the plume entrains fluid as a function of velocity, which is in turn a function of height. Our measurements do not show significant variation in entrainment velocity with height (Fig. 8B, F), but are instead relatively constant. We may infer from this that the characteristic velocity of the plume was also relatively constant until a height of ~ 5000–6000 m. The effectively constant velocity suggests that buoyancy flux increased linearly with height (Ishimine 2007).

Assuming a typical volcanic plume entrainment coefficient $\alpha = 0.1$, entrainment velocities of ~ 3 m/s suggest a plume centerline velocity of ~ 30 m/s, a reasonable value based upon plume models (Suzuki and Koyaguchi 2015). As the turbulence intensity should scale with but not exceed the centerline velocity, the turbulence intensity should indicate a minimum value for the interior velocity (e.g., the eddy rotation speed of the margins is comparable to the interior centerline velocity; Fig. 6). Our values of $U' =$ ~ 50 m/s thus suggest characteristic plume velocities U of ~ 50 m/s. Assuming that U' is representative of the centerline velocity, the ratio of entrainment velocity to U' as a function of height provides an estimate of the entrainment coefficient α as a function of height (Fig. 8D, H). Interestingly the profiles of α for both clips are on the order of 0.06 and are lower than most values for buoyant plumes; indeed, they are in closer agreement with the values for jets (e.g., Aubry et al. 2017a; Kaminski et al. 2005). That is, the value of α for negatively buoyant jets (Kaminski et al. 2005) is a better estimate of the entrainment coefficient, at least for the plume studied here, than the value typically used in volcanological studies (e.g., Aubry et al. 2017a). Two possible reasons for this very low value are that the measurement of volumetric entrainment rate (and thus entrainment velocity) is too low and that the measured turbulence intensity is too high; investigating why the apparent entrainment coefficient is low warrants future study.

Importance of 3D measurements of entrainment and application to plume modeling

The measurements presented in this study provide previously unavailable quantitative insights into plume behavior. These include measurements of the 4D (3 spatial dimensions and time) surface morphology of the plume, its 3D turbulent velocity field, entrainment into the plume, and the time- and length scales over which entrainment varies. These parameters can be used for model validation or assessment; for example, matching the characteristic surface "roughness" of the observed plume with a 3D model would help validate the model's calculation of turbulent length and timescales (e.g., Suzuki et al. 2005; Esposti Ongaro and Cerminara 2016). Similarly, the results could be compared against a 1D model such as Plumeria (Mastin 2007) to better constrain eruption source parameters including vent size and eruption rate. In addition, comparison of measured and modeled entrainment rates can be used to develop more sophisticated conceptual or quantitative insights into the interior velocity structures of eruption columns; these regions cannot be observed directly, but they ultimately determine buoyant or non-buoyant plume behavior (e.g., Carazzo et al. 2008b; Andrews and Gardner 2009; Jessop et al. 2016). Estimates of entrainment (or entrainment velocity) made using only the 2D velocity fields are systematically about half those made using the 3D technique. This difference is a result of the 2D calculation effectively being the sum of the 2D velocity field within regions of negative divergence. By excluding the velocity component parallel to the viewing angle, this method minimizes the contribution of the vectors that most actively entrain in the 3D measurement. Further work is required to determine if the factor of 2 difference between the 2D and 3D measurements is specific to these particular film clips, or if it is general.

The analytical techniques described in this paper can be applied to long duration video observations of explosive volcanic eruptions. Although we focused on a vent-sourced buoyant plume, our method could be applied to coignimbrite plumes or pyroclastic density currents. Neither total file size nor required processing time preclude conducting this type of analysis for multiple hours of eruption footage. This is particularly true when considered in the context of numerical models requiring 100s or 1000 s of hours of high-performance computing time. Video acquired in recent years, particularly 4K high-definition video, should be well-suited to this method as these new data sources have lens data encoded within their constituent files and are frequently geolocated and time-stamped.

Conclusions

Air entrainment into explosive eruption plumes modulates the dynamic transition between the buoyant and collapsing endmember regimes of eruption behavior. Consequently, understanding entrainment rate, together with the turbulent timescales and length scales over which that rate varies, is required for improved models and forecasts of eruption dynamics. We demonstrate that 3D measurements of turbulent air entrainment can be made from film or video observations of eruption columns using a combination of feature tracking velocimetry and single-camera surface reconstruction; this technique can be applied to recent as well as historic film of eruptions. We show that the 22 March 1944 Vesuvius eruption column entrained air at a rate of 1–3 × 10^8 m^3s^{-1} during the filmed portions of the afternoon. That range corresponds to an entrainment velocity of 2.8–2.9 m/s, with about one-third of the plume surface actively entraining at any given time. Entrainment velocity does not vary systematically with height, suggesting that the characteristic velocity of the plume interior is roughly constant from the vent to a height of 5000–5500 m. Interestingly, the entrainment velocity has a magnitude on the order of 6% of the magnitude of the turbulent intensity. This may indicate that the turbulent intensity as measured on the plume surface is a proxy for the characteristic velocity of the unobservable plume interior.

Supplementary Information The online version contains supplementary material available at https://doi.org/10.1007/s00445-024-01703-1.

Acknowledgements We thank M. Benage, M. Jellinek, J. Gilchrist, and C. Rowell for helpful discussions regarding turbulent volcanic plumes. Helpful reviews by T.J. Aubry and an anonymous reviewer improved this manuscript. The Natural History Research Experience REU program helped reinvigorate this project.

Funding This research was funded by NSF awards EAR-1852471 to BJA and OCE-1560088 to E. Cottrell and G. Hunt and the Smithsonian Institution National Museum of Natural History.

References

Andrews BJ (2014) Dispersal and air entrainment in unconfined dilute pyroclastic density currents. Bull Volcanol 76(9):852

Andrews BJ (2019) Recognizing unsteadiness in the transport systems of dilute pyroclastic density currents. Bull Volcanol 81(2):5. https://doi.org/10.1007/s00445-018-1266-5

Andrews BJ, Cardenas MB, Bennett PC (2011) Analysis of turbulent non-isothermal mixing between a jet and cooler ambient water using thermal imagery. Geochem Geophys Geosyst 12:Q07022. https://doi.org/10.1029/2011GC003530

Andrews BJ, Gardner JE (2009) Turbulent dynamics of the 18 May 1980 Mount St. Helens eruption column. Geology 37:895–898

Andrews BJ, Gardner JE, Tait S, Ponomareva V, Melekestsev IV (2007) Dynamics of the 1800 14C yr BP caldera-forming eruption of Ksudach Volcano, Kamchatka, Russia. In: Eichelberger J, Gordeev E, Kasahara M, Izbekov P, Lees J (eds) Volcanism and subduction: the Kamchatka region, vol 172. Geophysical Monograph, pp 325–342

Andrews BJ, Manga M (2012) Turbulence, sedimentation, and coignimbrite partitioning in dilute pyroclastic density currents. J Volcanol Geotherm Res 225:30–44. https://doi.org/10.1029/2011GL050475

Aubry TJ, Carazzo G, Jellinek AM (2017a) Turbulent entrainment into volcanic plumes: new constraints from laboratory experiments on buoyant jets rising in a stratified crossflow. Geophys Res Lett. https://doi.org/10.1002/2017GL075069

Aubry TJ, Engwell SL, Bonadonna C, Carazzo G, Scollo S, Van Eaton AR, Taylor IA, Jessop D, Eychenne J, Gouhier M, Mastin LG, Wallace KL, Biass S, Bursik M, Grainger RG, Jellinek AM, Schmidt A (2021) The Independent Volcanic Eruption Source Parameter Archive (IVESPA, version 1.0): a new observational database to support explosive eruptive column model validation and development. J Volcanol Geotherm Res. https://doi.org/10.1016/j.jvolgeores.2021.107295

Aubry TJ, Jellinek AM (2018) New insights on entrainment and condensation in volcanic plumes: constraints from independent observations of explosive eruptions and implications for assessing their impacts. Earth Planet Sci Lett 490:132–142. https://doi.org/10.1016/j.epsl.2018.03.028

Aubry TJ, Jellinek AM, Carazzo G, Gallo R, Hatcher K, Dunning J (2017b) A new analytical scaling for turbulent wind-bent plumes: comparison of scaling laws with analog experiments and a new database of eruptive conditions for predicting the height of volcanic plumes. J Volcanol Geotherm Res 343:233–251. https://doi.org/10.1016/j.jvolgeores.2017.07.006

Benage MC, Andrews BJ, Gooding T (2019) Turbulent structure and particle clustering in analog volcanic jets. Am Geophys Union Fall Meeting, pp V31A–V305A

Benage MC, Dufek J, Mothes P (2016) Quantifying entrainment in pyroclastic density currents from the Tungurahua eruption, Ecuador: integrating field proxies with numerical simulations. Geophys Res Lett 43:6932–6941. https://doi.org/10.1002/2016GL069527

Bernard PS, Wallace JM (2002) Turbulent flow: analysis, measurement, and prediction. Wiley, Hoboken, New Jersey, p 512

Bombrun M, Jessop D, Harris A, Barra V (2018) An algorithm for the detection and characterization of volcanic plumes using thermal camera imagery. J Volcanol Geotherm Re 352:26–37. https://doi.org/10.1016/j.jvolgeores.2018.01.006

Burgisser A, Bergantz GW, Breidenthal RE (2005) Addressing the complexity in laboratory experiments: the scaling of dilute multiphase flows in magmatic systems. J Volcanol Geotherm Res 141:245–265. https://doi.org/10.1016/j.jvolgeores.2004.11.001

Bursik M (2001) Effect of wind on the rise height of volcanic plumes. Geophys Res Lett 28:3821–3824. https://doi.org/10.1029/2001GL013393

Carazzo G, Girault F, Aubry TJ, Bouquerel H, Kaminski E (2014) Laboratory experiments of forced plumes in a density-stratified crossflow and implications for volcanic plumes. Geophys Res Lett 41:8759–8766. https://doi.org/10.1002/2014GL061887

Carazzo G, Jellinek AM (2012) A new view of the dynamics, stability and longevity of volcanic clouds. Earth Planet Sci Lett 325:39–51. https://doi.org/10.1016/j.epsl.2012.01.025

Carazzo G, Kaminski E, Tait S (2006) The route to self-similarity in turbulent jets and plumes. J Fluid Mech 547:137–148. https://doi.org/10.1017/S002211200500683X

Carazzo G, Kaminski E, Tait S (2008a) On the dynamics of volcanic columns: a comparison of field data with a new model of negatively buoyant jets. J Volcanol Geotherm Res 178:94–103

Carazzo G, Kaminski E, Tait S (2008b) ON the rise of turbulent plumes: quantitative effects of variable entrainment for submarine hydrothermal vents, terrestrial and extra terrestrial explosive volcanism. J Geophys Res 110:B09201. https://doi.org/10.1029/2007B005458

Carey SN, Sparks RSJ (1986) Quantitative models of the fallout and dispersal of tephra from volcanic eruption columns. Bull Volcanol 48:109–125

Cerminara M, Esposti Ongaro T, Neri A (2016) Large eddy simulation of gas-particle kinematic decoupling and turbulent entrainment in volcanic plumes. J Volcanol Geotherm Res 326:143–171. https://doi.org/10.1016/j.jvolgeores.2016.06.018

Chen CJ, Rodi W (1980). Vertical turbulent buoyant jets: a review of experimental data. NASA STI/Recon Technical Report A, 80, 23,073.

Christiansen RL, Peterson DW (1981) Chronology of the 1980 activity of Mount Saint Helens, Washington. In: Lipman PW, Mullineaux DR (eds) The 1980 eruptions of Mount St. Helens. USGS Professional Paper 1250, Washington, pp 17–30

Cole PD, Scarpatti C (2010) The 1944 eruption of Vesuvius, Italy: combining contemporary accounts and field studies for a new volcanological reconstruction. Geol Mag 147:391–415. https://doi.org/10.1017/S0016756809990495

Criswell W (1987) Chronology and pyroclastic stratigraphy of the May 18, 1980, eruption of Mount St. Helens, Washington. J Geophys Res 92(10):237–10266. https://doi.org/10.1029/JB092iB10p10237

Cubellis E, Marturano A, Lucia P (2016) The last Vesuvius eruption in March 1944: reconstruction of the eruptive dynamic and its impact on the environment and people through witness reports and volcanological evidence. Nat Hazards 82:95–121. https://doi.org/10.1007/s11069-016-2182-7

Degruyter W, Bonadonna C (2013) Impact of wind on the condition for column collapse of volcanic plumes. Earth Planet Sci Lett 377:218–226. https://doi.org/10.1016/j.epsl.2013.06.041

Devenish B, Rooney G, Webster H, Thomson D (2010) The entrainment rate for buoyant plumes in a crossflow. Bound-Layer Meteorol 134:411–439. https://doi.org/10.1007/s10546-009-9464-5

Esposti Ongaro T, Cerminara M (2016) Non-equilibrium processes in ash-laden volcanic plumes: new insights from 3D multiphase flow simulations. J Volcanol Geotherm Res 326:127–142

Gilchrist JT, Jellinek AM (2021) Sediment waves and the gravitational stability of volcanic jets. Bull Volcanol 83:64. https://doi.org/10.1007/s00445-021-01472-1)

Global Volcanism Program, 2013. Vesuvius (211020) in volcanoes of the world, v. 4.9.0 (04 Jun 2020). Venzke, E (ed.). Smithsonian Institution. Downloaded 21 Aug 2020 (https://volcano.si.edu/volcano.cfm?vn=211020). https://doi.org/10.5479/si.GVP.VOTW4-2013

Harker M, O'Leary P (2013) Direct redularized surface reconstruction from gradients for Industrial Photometric Stereo. Comput Ind 64:1221–1228. https://doi.org/10.1016/j.compind.2013.03.013

Hewett T, Fay J, Hoult D (1971) Laboratory experiments of smokestack plumes in a stable atmosphere. Atmos Environ 5:767–789. https://doi.org/10.1016/0004-6981(71)90028-X

Ishimine Y (2007) A simple integral model of buoyancy-generating plumes and its application to volcanic eruption columns. J Geophys Res 112:B03210. https://doi.org/10.1029/2006JB004274

Jessop D, Gilchrist J, Jellinek AM, Roche O (2016) Are eruptions from linear fissures and caldera ring dykes more likely to produce pyroclastic flows? Earth Planet Sci Lett 454:142–153. https://doi.org/10.1016/j.epsl.2016.09.005

Jessop DE, Jellinek AM (2014) Effects of particle mixtures and nozzle geometry on entrainment into volcanic jets. Geophys Res Lett 41:3858–3863. https://doi.org/10.1002/2014GL060059

Kaminski E, Tait S, Carazzo G (2005) Turbulent entrainment in jets with arbitrary buoyancy. J Fluid Mech 526:361–376. https://doi.org/10.1017/S0022112004003209

Mastin L, Pavolonis M, Engwell S, et al. (2022) Progress in protecting air travel from volcanic ash clouds. Bull Volcanol 84, 9. https://doi.org/10.1007/s00445-021-01511-x

Mastin LG (2007) A user-friendly one-dimensional model for wet volcanic plumes. Geochem Geophys Geosyst 24. https://doi.org/10.1029/2006GC001455

Mastin LG (2014) Testing the accuracy of a 1-D volcanic plume model in estimating mass eruption rate. J Geophys Res-Atmos 119:2474–2495. https://doi.org/10.1002/2013JD020604

Mastin LG, Ghiorso MS (2000) A numerical program for steady-state flow of magma-gas mixtures through vertical eruptive conduits. USGS Open File Report 00-209

Mastin LG, Guffanti M, Servranckx R, Webley P, Barsotti S, Dean K, Durant A, Ewert JW, Neri A, Rose WI, Schneider D, Siebert L, Stunder B, Swanson G, Tupper A, Volentik A, Waythomas CF (2009) A multidisciplinary effort to assign realistic source parameters to models of volcanic ash-cloud transport and dispersion during eruptions. J Volcanol Geotherm Res 186:10–21. https://doi.org/10.1016/j.jvolgeores.2009.01.008

Mastin LG, Randall MJ, Schwaiger HF, Denlinger RP (2013) User's guide and reference to Ash3d—A three-dimensional model for Eulerian atmospheric tephra transport and deposition. USGS Open-File Report 2013–1122, p 48 http://pubs.usgs.gov/of/2013/1122/

Morton BR, Taylor G, Turner JS (1956) Turbulent gravitational convection from maintained and instantaneous sources. Proc Roy Soc London A: Math Phys Eng Sci 234:1–23. https://doi.org/10.1098/rspa.1956.0011

Muppidi S, Mahesh K (2008) Direct numerical simulation of passive scalar transport in transverse jets. J Fluid Mech 598:335–360. https://doi.org/10.1017/S0022112007000055

Neri A, Dobran F (1994) Influence of eruption parameters on the thermofluid dynamics of collapsing volcanic columns. J Geophys Res 99:11833–11857

Neri A, Esposti Ongaro T, Macedonio G, Gidaspow D (2003) Multiparticle simulation of collapsing volcanic columns and pyroclastic flow. J Geophys Res 108:B4. https://doi.org/10.1029/2001JB000508

Pope SB (2000) Turbulent flows. Cambridge University Press. https://doi.org/10.1017/CBO9780511840531

Pouget S, Bursik M, Singla P, Singh T (2016) Sensitivity analysis of a one-dimensional model of a volcanic plume with particle fallout and collapse behavior. J Volcanol Geotherm Res 326:43–53. https://doi.org/10.1016/j.jvolgeores.2016.02.018

Saffaraval F, Solovitz SA, Ogden DE, Mastin LG (2012) Impact of reduced near-field entrainment of overpressured volcanic jets on plume development. J Geophys Res 117:B05209

Scott WE, Hoblitt RP, Torres RC, Self S, Martinez MML, Nillos T Jr (1996) Pyroclastic flows of the June 15, 1991, climactic eruption of Mount Pinatubo. In: Newhall CG, Punongbayan RS (eds) Fire and mud: eruptions and lahars of Mount Pinatubo, Philippines: Seattle. University of Washington Press, pp 545–570

Sparks RSJ (1986) The dimensions and dynamics of volcanic eruption columns. Bull Volcanol 48:3–15. https://doi.org/10.1007/BF01073509

Sparks RSJ, Wilson L (1982) Explosive volcanic eruptions. V, Observations of plume dynamics during the 1978 Soufriere eruption, St. VIncent Roy. Astron Soc Geophys J 69:55–570

Suzuki Y, Koyaguchi T (2015) Effects of wind on entrainment in volcanic plumes. J Geophys Res Solid Earth 120:6122–6140. https://doi.org/10.1002/2015JB012208

Suzuki YK, Koyaguchi T, Ogawa M, Hachisu I (2005) A numerical study of turbulent mixing in eruption clouds using a three dimensional fluid dynamics model. J Geophys Res 110:B08201. https://doi.org/10.1029/2004JB003460

Turner JS (1962) The starting plume in neutral surroundings. J Fluid Mech 13:356–368

Veitch G, Woods AW (2000) Particle recycling and oscillations of volcanic eruption columns. J Geophys Res 105:2829–2842

Wilson L, Sparks RSJ, Huang TC, Watkins ND (1978) The control of eruption column heights by eruption energetics and dynamics. J Geophys Res 83:1829–1836

Woods AW (1988) The fluid dynamics and thermodynamics of eruption columns. Bull Volcanol 50:169–193. https://doi.org/10.1007/BF01079681

Woods AW, Kienle J (1994) The dynamics and thermodynamics of volcanic clouds: theory and observations from the April 15 and April 21, 1990 eruptions of redoubt volcano, Alaska. J Volcanol Geotherm Res 62:273–299. https://doi.org/10.1016/0377-0273(94)90037-X